Chapter 6

ULTIMATE BEARING CAPACITY FACTORS FOR RING FOOTING ON ROCKMASS DUE TO VARIOUS LOADING POSITIONS

6.1 INTRODUCTION

The ultimate bearing capacity of ring footings subjected to complete and partial loading was analyzed in the preceding chapters. The ring footings were placed on homogenous as well as different combinations of layered soils. However, in many practical situations, ring footings are also constructed over rock stratum. In contrast to the soils, the yield envelope that describes the rock strength behaviour is highly nonlinear in $\tau-\sigma_n$ and $\sigma_1-\sigma_3$ spaces. Hence, nonlinear yield criteria are to be employed for predicting the ring behavior located on highly nonlinear geomaterial, i.e., rock. The Hoek-Brown yield criterion (Hoek and Brown, 1980, 1988, 1997; Hoek et al., 2002) is the most preferred yield criterion for assessing rock mass failure. By using HB yield criterion, several stability problems in rock medium are elaborately studied; for example, designing underground openings and caverns (Sakurai, 1993; Martin and Maybee, 2000; Swift and Reddish, 2005), computing the bearing capacity of strip footing (Serrano & Olalla, 1998a, 1998b; Yang and Yin, 2005; Merifield et al., 2006; Saada et al., 2008), assessing the rock slope stability (You et al., 2000; Yang and Yin, 2004; Li et al., 2008).

To understand the behavior of axisymmetric footing (ring/circular) on rocks, a few studies were conducted earlier with the help of elastoplastic finite-element method (Clausen, 2013), finite element limit analysis in conjunction with the interior point method (Chakraborty and Kumar, 2015), method of stress characteristics (Keshavarz

and Kumar, 2018, 2021), FELA based Optum G2 software (Xiao et al., 2020). In these studies, the impact of the rock strength and the geometry of the ring were rigorously verified by considering the uniform distribution of the load over the entire footing area. However, there are several occasions where the loads are partially placed over the annular section of the footing. However, as per the authors' findings, no literature seems to exist that rigorously assessed the behaviour of ring footing resting on rock mass and subjected to partial loading. This motivates the authors for carrying out the present research

This study aims in understanding the effect of partial loading on the load withstand capacity of ring footing placed over rock mass with the help of lower bound finite elements limit analysis in conjunction with nonlinear optimization. The numerical simulations are carried out by placing the load over three different positions of the footing, namely, the inner half, middle half, and outer half of the footing. The rock stratum is modeled by using the three-dimensional generalized Hoek-Brown (GHB) yield criterion. To avoid numerical complexities, the sharp corners present in the GHB are further smoothened by using a trigonometric approximation in the deviatoric plane and a quasi-hyperbolic approximation in the meridional planes. The interior point method (IPM) based on the logarithmic barrier function, as proposed by Krabbenhoft and Damkilde (2003), is employed for encountering the nonlinear yield constraints in the LB-FELA formulations. The results are presented in terms of nondimensional factors with respect to varying ring geometry, surcharge pressures, rock strength, and loading position. The failure patterns are drawn for a few cases on the basis of the deviatoric stress ratio. The obtained solutions are compared with the results available in the published literature.

6.2 PROBLEM STATEMENT AND DOMAIN

A rigid ring footing with an outer radius, r_0, and an inner radius, r_i, is placed over a homogenous rock medium. The rock layer is assumed to be weightless, perfectly plastic, governs by the generalized Hoek-Brown yield criterion, associative flow rule, and stress independent strength parameters. The interface between the footing and the rock mass is perfectly rough. The surcharge pressure acts normal to the ground surface and is spread over the outer as well as the hollow portion of the ring footing. The load is symmetrically applied over a limited portion of the annular surface. Along with the loading on the entire plan area (L_0), three different partial loading configurations are considered herein. They are: (i) inner half loading (L_1), (ii) middle half loading (L_2), and (iii) outer half loading (L_3). Figure 6.1a shows the chosen loading type and Figure 6.1b displays the three-dimensional (3D) form of the problem. About the central axis of the footing, the material properties, geometrical configuration, loading arrangement, and boundary constraints of the underlying rockmass and overlying ring foundation are symmetric, and, therefore, the 3D problem is idealized to be of axisymmetric (2D) in nature, as shown in Figure 6.1c. The cylindrical coordinates (r–θ–z) are explicitly used in the present analysis. The rock layer is assumed to consist of either intact rocks or rock masses without any preferential direction of slippage; this assumption provides flexibility in the usage of an isotropic yield criterion. It is intended to rigorously determine the lower bound bearing capacity of the ring footing corresponding to various combinations of ring geometry, applied surcharge loading, and the rock strength. The distribution of deviatoric stress ratio at the collapse state is also drawn.

Considering the axisymmetricity of the problem, only one-half of the problem domain in two-dimensional stress space (r–z) is taken for the analysis. Figure 6.1c

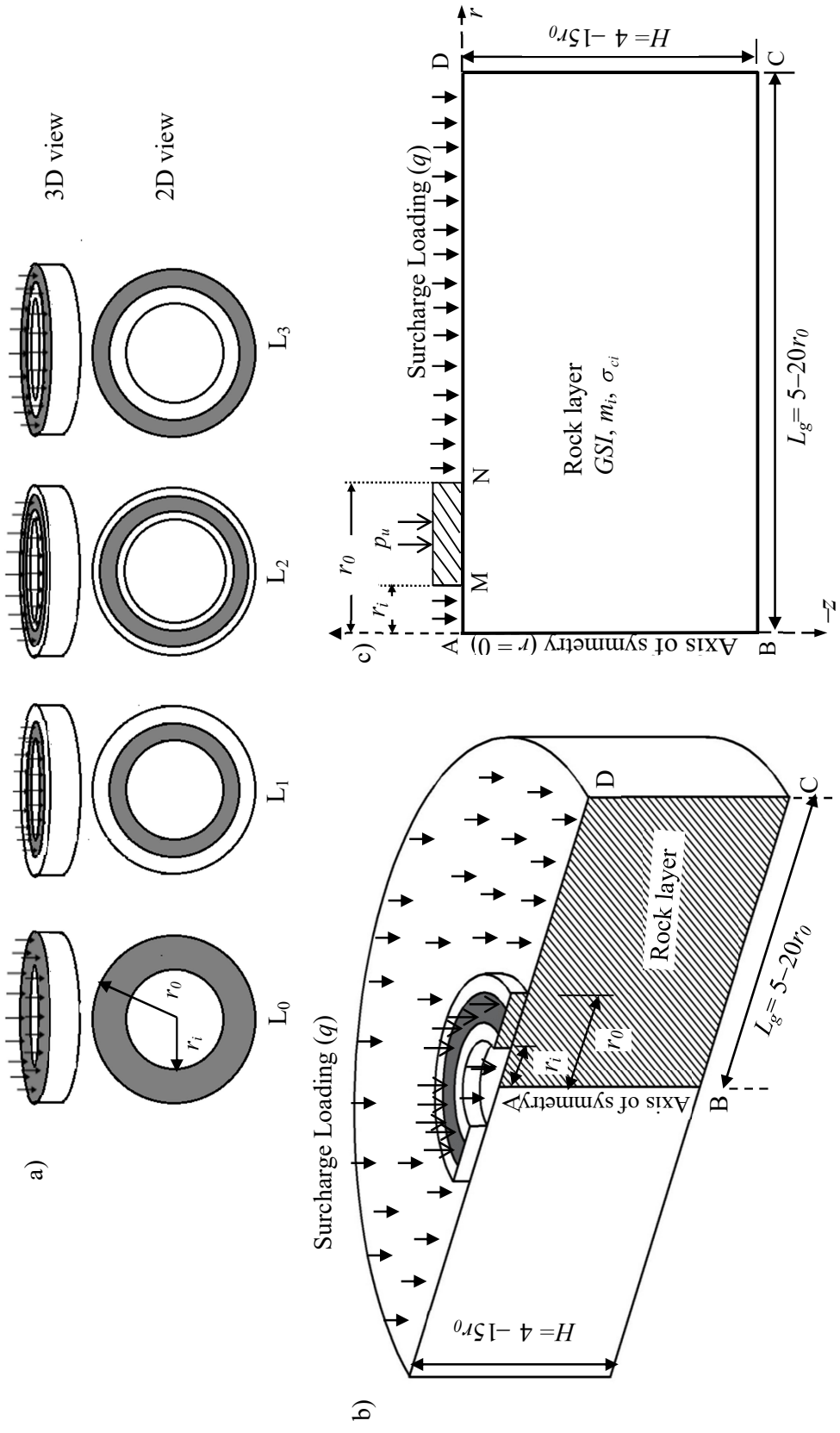

Figure 6.1 a) Different configurations of loadings applied on the rough ring footing rested over homogenous rocks, as represented in b) three-dimensional form, and c) two-dimensional axisymmetric form.

represents symmetrical plane of domain and associated stress boundary conditions. The domain size is chosen sufficiently high such that the failure zones are well contained within the defined domain boundaries and any further enlargement of the domain does not affect the result of analysis. The radial and vertical extent of the domain is taken between $5r_0$ to $20r_0$ and $4r_0$ to $15r_0$, respectively. A relatively larger domain is taken either when the simulations are carried over the stronger rockmass or surcharge pressure is applied.

The domain is discretized with three-nodded triangular elements. To account for the sudden change in stress direction at the footing edge, a non-uniform mesh is constructed by reducing the element size near the footing edge. A typical mesh pattern employed in the analysis is shown in Figure 6.2. The rock strength and the ring geometry influences the domain size and mesh pattern.

6.3 HOEK-BROWN YIELD CRITERION

Owing to its wide usage, better predictiveness, easiness of handling, Hoek-Brown yield criterion is regarded as the most preferred yield criterion over other alternative rock strength-determining models. Based on a large number of triaxial tests on several varieties of rock samples, Hoek and Brown (1980) initially proposed the original Hoek-Brown (OHB) criterion which nonlinearly relates the major (σ_1) and minor (σ_3) principal stresses at failure state as expressed by:

OHB criterion: $(\sigma_1 - \sigma_3)^2 + m\sigma_1\sigma_{ci} = s\sigma_{ci}^2$ (6.1a)

In above expression, (i) σ_{ci} indicates the uniaxial compressive strength of the intact rock material, (ii) the nondimensional strength parameter, *m* and *s* are indirectly analogous to the frictional and the cohesive strength of the rock, respectively; these parameters depend upon the rock properties before being subjected to external loadings. The

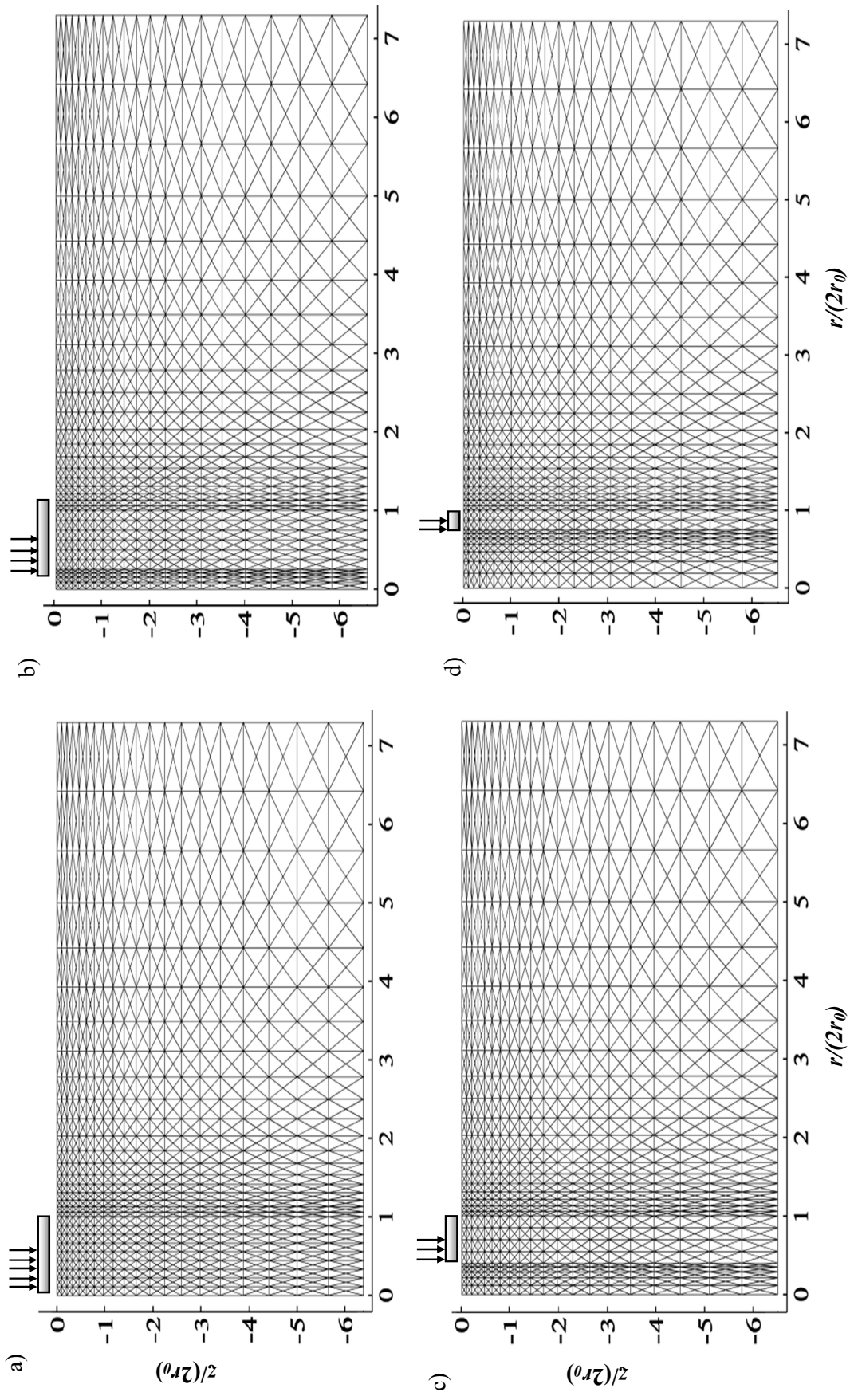

Figure 6.2 Mesh used for the ring footing for four different radius ratios: a) r_i/r_0= 0; b) r_i/r_0= 0.25; c) r_i/r_0= 0.50 and d) r_i/r_0= 0.75.

empirical parameter *s* indicates the extent of rock fracturing; $s = 0$ denotes heavily fractured rock mass and $s = 1$ refers to intact rock mass. The higher the degree of fragmentation the lower the value of *m* and *s*. These rock strength parameters are the direct function of mineralogy and discontinuities present in the rock. In this context, it is worth mentioning that one of the reasons behind the popularity of HB criterion can be attributed to the fact that the required strength parameters can be easily measured by (i) uniaxial testing of rock samples, (ii) mineralogical examination, and (iii) characterization of rock discontinuities.

Later, the OHB criterion was suitably modified by Hoek and Brown (1997), and the generalized Hoek-Brown (GHB) criterion was recommended to address the jointed and fractured rock mass behavior more realistically:

GHB criterion: $(\sigma_1 - \sigma_3)^{1/\alpha} + m_b \sigma_1 \sigma_{ci}^{(1-\alpha)/\alpha} = s\sigma_{ci}^{1/\alpha}$ (6.1b)

For accounting the broken rock mass the dimensionless terms, m_b and α, were introduced in the GHB criteria on the basis of the *GSI* (Geological Strength Index) classification system. The terms m_b, *s*, and α are defined as follows:

$$m_b = m_i \exp\left(\frac{GSI - 100}{28 - 14D_f}\right) \tag{6.2a}$$

$$s = \exp\left(\frac{GSI - 100}{9 - 3D_f}\right) \tag{6.2b}$$

$$\alpha = \frac{1}{2} + \frac{1}{6}\left(\exp\left(\frac{-GSI}{15}\right) - \exp\left(\frac{-20}{3}\right)\right) \tag{6.2c}$$

Here, (i) m_i is the *m* value for intact rock, which depends on rock type and surface texture. For instance, the values of m_i for marble (coarse metamorphic rock) and granite (coarse igneous rock) range between 6-12 and 30-35, respectively.

(ii) D_f represents the disturbance factor which shows the extent of disturbance of the rock mass due to weathering, blast damage, and stress relief; the value of D_f ranges between 0 (undisturbed rock sample) and 1 (disturbed rock sample), and

(iii) *GSI* represents a number depending on two geological observations, namely, the surface quality and the interlocking among the rock blocks. The value of *GSI* varies from 10 (representing very poor-quality rock mass) to 100 (characterizing extremely strong unjointed rock mass). The *GSI* value is maximum for massive rock with a fresh unweathered surface, whereas, the *GSI* value is minimum for laminated/sheared rocks having slickensided, highly weathered surfaces infused with soft clay infills. For the practical values of GSI (10 to 100), the exponent α varies between 0.59 and 0.50; corresponding to GSI = 100, α becomes equal to 0.5 which turns GHB criterion into OHB. In terms of three stress invariants (σ_m –$\overline{\sigma}$–θ) the yield criteria mentioned in Equation (6.1) can further be rewritten as

OHB criterion:

$$f(\boldsymbol{\sigma}) = (2\overline{\sigma}\cos\theta)^2 - m_b\sigma_{ci}\overline{\sigma}\left(\frac{\sin\theta}{\sqrt{3}} - \cos\theta\right) + m_b\sigma_{ci}\sigma_m - s\sigma_{ci}^2 = 0 \qquad (6.3a)$$

GHB criterion:

$$f(\boldsymbol{\sigma}) = (2\overline{\sigma}\cos\theta)^{1/\alpha} - m_b\sigma_{ci}^{(1-\alpha)/\alpha}\overline{\sigma}\left(\frac{\sin\theta}{\sqrt{3}} - \cos\theta\right) + m_b\sigma_{ci}^{(1-\alpha)/\alpha}\sigma_m - s\sigma_{ci}^{1/\alpha} = 0 \qquad (6.3b)$$

Here, σ_m, $\overline{\sigma}$ and θ are the hydrostatic stress, deviatoric stress and the Lode's angle, respectively, and are expressed in Section 3.2.9.

It is well observed that the assumption of choosing $\alpha = 0.5$ provides an unsafe solution for *GSI* < 40. The previous studies (Chakraborty and Kumar, 2016, 2019) suggest that for a lower value of *GSI*, the bearing capacity can be overestimated even to

an extent of 200-250%. In the present analysis, the GHB criterion which considers the true variation of α is employed.

Figure 6.3 illustrates the form of GHB criterion in the three-dimensional stress spaces for different combinations of *GSI* and m_i. This figure clearly gives an impression that the size of GHB curved pyramids reduces with the decrement in *GSI* and m_i. It is further noted that the yield envelopes possess six edge discontinuities and one tip discontinuity.

6.4 ANALYSIS

The LB-FELA has been employed in conjunction with finite element and non-linear optimization. to determine ultimate bearing capacity (p_u). The steps for equality constrains and objective functions are already discussed in Section 3.2. For nonlinear optimization, gradient and Hessian of GHB yield function are required. Appendix D contains gradient and Hessian of GHB yield function.

6.5 SMOOTHENING OF THE GHB CRITERION

For axisymmetric problems, there is a high probability of the stress state being located in the vicinity of the yield surface corners. The gradient and Hessian of the yield function will no longer remain to be unique at these singular points. This eventually creates computational complexities. To remove such irregularities, the yield surface is adequately smoothened in the π ($\overline{\sigma}-\theta$) and the meridian ($\sigma_m-\overline{\sigma}$) planes by means of the quasi-hyperbolic approach (Merifield et al., 2006) and trigonometric approximation (Sloan and Booker, 1986 and Chakraborty and Kumar, 2014), respectively. The smoothened GHB criterion takes the following form:

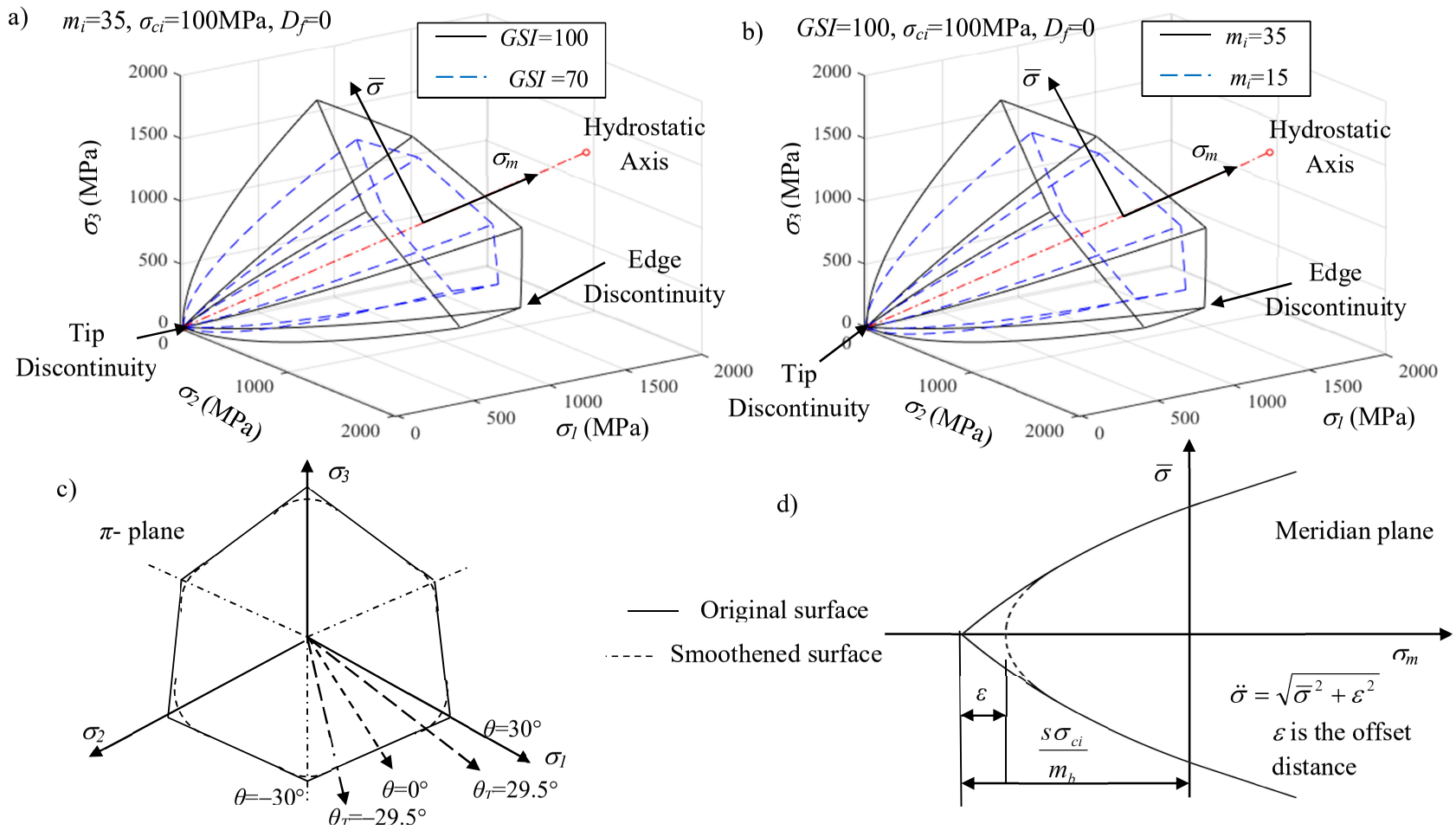

Figure 6.3 (a-b) Representation of the 3-D GHB criterion with different *GSI* and m_i – a) m_i=35 and varying *GSI*; b) *GSI* =100 and varying m_i; (c-d) removal of discontinuities on the 3-D GHB yield surface – c) smoothening edge discontinuities in the octahedral plane; and d) rounding-off tip discontinuity in the meridian plane

$$f(\boldsymbol{\sigma}) = (2\ddot{\sigma}\cos\theta)^{1/\alpha} - m_b\sigma_{ci}^{(1-\alpha)/\alpha}\ddot{\sigma}\left(\frac{\sin\theta}{\sqrt{3}} - \cos\theta\right) + m_b\sigma_{ci}^{(1-\alpha)/\alpha}\sigma_m - s\sigma_{ci}^{1/\alpha} = 0 \text{ for } |\theta| < \theta_T \tag{6.4a}$$

$$= m_b\sigma_{ci}^{(1-\alpha)/\alpha}\sigma_m - m_b\sigma_{ci}^{(1-\alpha)/\alpha}\ddot{\sigma}(A + B\sin 3\theta + C\sin^2 3\theta) - s\sigma_{ci}^{1/\alpha} = 0 \quad \text{for } |\theta| \geq \theta_T \tag{6.4b}$$

Here, (i) $\ddot{\sigma} = \sqrt{\bar{\sigma}^2 + \varepsilon^2}$; ε is the offset distance between the original tip point and the smoothened surface along the $\bar{\sigma}$ axis and is determined as: $\varepsilon = \min(\delta, \mu\rho)$; where, the values of δ, μ, and ρ are chosen from:

$$\rho\left|-2\rho + (\rho m_b\sigma_{ci}^{(1-\alpha)/\alpha} + s\sigma_{ci}^{1/\alpha})^{\alpha} = 0;\ \delta = 10^{-6}\ ;\ \mu = 10^{-1}\right. \tag{6.5}$$

(ii) the values of *A*, *B*, and *C* are numerically determined from the construction of C^2 continuous modified smoothened yield surface in the $\pi-$ plane on the basis of the fact that:

(a) the value of $\bar{\sigma}$, $\frac{\partial\bar{\sigma}}{\partial\theta}$ and $\frac{\partial^2\bar{\sigma}}{\partial\theta^2}$ derived from the modified as well the parent GHB yield surface are made to be the same at the transition Lode angle (θ_T), and

(b) $\frac{\partial\bar{\sigma}}{\partial\theta}$ (at $\theta = \pm 30°$) = 0.

The following yield function satisfies all the requirements as mentioned earlier.

$$f(\boldsymbol{\sigma}) = m_b\sigma_{ci}^{(1-\alpha)/\alpha}\sigma_m - m_b\sigma_{ci}^{(1-\alpha)/\alpha}\ddot{\sigma}(A + B\sin 3\theta + C\sin^2 3\theta) - s\sigma_{ci}^{1/\alpha} = 0 \tag{6.6}$$

$$(A + B\langle\theta\rangle\sin 3\theta + C\sin^2 3\theta) = (m_b\sigma_{ci}^{(1-\alpha)/\alpha}\sigma_m - s\sigma_{ci}^2)/(m_b\sigma_{ci}^{(1-\alpha)/\alpha}\ddot{\sigma}) \tag{6.7}$$

By equating the three equations given in three conditions, the value of *A*, *B* and *C* can be expressed as:

$$A = \left(\frac{R\sigma_m - s\sigma_{ci}^2}{162R\ddot{\sigma}^2\cos^2 3\theta}\right)\left(2\sin^2 3\theta + \left(\frac{R\sigma_m - s\sigma_{ci}^2}{3R\ddot{\sigma}^2\cos 3\theta}\right)(N_1\langle\theta\rangle\sin 3\theta) - \sin 3\theta\right)T + \frac{R\sigma_m - s\sigma_{ci}^2}{R\ddot{\sigma}} \tag{6.8}$$

$$B = -2\left(\frac{R\sigma_m - s\sigma_{ci}^2}{R}\right)\left(\frac{\langle\theta\rangle \sin 3\theta}{162\ddot{\sigma}^2 \cos^2 3\theta}\right)T - \frac{R\sigma_m - s\sigma_{ci}^2}{3R\ddot{\sigma}^2 \cos 3\theta} N_1 \tag{6.9}$$

$$C = \left(\frac{R\sigma_m - s\sigma_{ci}^2}{162R\ddot{\sigma}^2 \cos^2 3\theta}\right)T \tag{6.10}$$

where, $N_1 = \dfrac{N_2(2\ddot{\sigma}\langle\theta\rangle \sin\theta) + R\ddot{\sigma}\left(\dfrac{\cos\theta}{\sqrt{3}} + \langle\theta\rangle \sin\theta\right)}{N_2(2\cos\theta) - R\ddot{\sigma}\left(\dfrac{\langle\theta\rangle \sin\theta}{\sqrt{3}}\cos\theta\right)}$

$$N_2 = \frac{1}{\alpha}(2\ddot{\sigma}\cos\theta)^{(1-\alpha)/\alpha}$$

$$R = m_b \sigma_{ci}^{(1-\alpha)/\alpha}$$

$$T = -\frac{\ddot{\sigma}}{\bar{\sigma}^4}(\bar{\sigma}^2 - \ddot{\sigma}^2)N_1^2 - \frac{2N_1^2}{\ddot{\sigma}} + \frac{27N_1}{\cos 3\theta} + N_2 MP_1 + N_3 MP_2 - RM(P_3 + P_4 + P_5 + P_6)$$

$$M = \frac{1}{\left[N_2(2\cos\theta) - R\left(\dfrac{\langle\theta\rangle \sin\theta}{\sqrt{3}} - \cos\theta\right)\right]}$$

$$P_1 = \left[2\cos\theta\left(\frac{\bar{\sigma}^2 - \ddot{\sigma}^2}{\ddot{\sigma}\bar{\sigma}^2}\right)\left(\frac{\partial\bar{\sigma}}{\partial\theta}\right)^2 - 4\langle\theta\rangle \sin\theta\left(\frac{\bar{\sigma}}{\ddot{\sigma}}\right)\left(\frac{\partial\bar{\sigma}}{\partial\theta}\right) - 2\ddot{\sigma}\cos\theta\right]$$

$$P_2 = \left(2\cos\theta\frac{\bar{\sigma}}{\ddot{\sigma}}\frac{\partial\bar{\sigma}}{\partial\theta} - 2\ddot{\sigma}\langle\theta\rangle \sin\theta\right)^2$$

$$P_3 = -\frac{\langle\theta\rangle \sin\theta}{\sqrt{3}} + \cos\theta$$

$$P_4 = \left(\frac{\cos\theta}{\sqrt{3}} + \langle\theta\rangle \sin\theta\right)\frac{\bar{\sigma}}{\ddot{\sigma}}\frac{\partial\bar{\sigma}}{\partial\theta}$$

$$P_5 = \left(\frac{\langle\theta\rangle \sin\theta}{\sqrt{3}} - \cos\theta\right)\left(\frac{\partial\bar{\sigma}}{\partial\theta}\right)^2\left(\frac{\bar{\sigma}^2 - \ddot{\sigma}^2}{\ddot{\sigma}\bar{\sigma}^2}\right)$$

$$P_6 = \left(\frac{\partial\bar{\sigma}}{\partial\theta}\right)\left(\frac{\cos\theta}{\sqrt{3}} + \langle\theta\rangle \sin\theta\right)$$

$\langle\theta\rangle$ is defined in Section 3.2.9.2.

The two smoothening parameters, ε and θ_T, control the degree of closeness of the modified GHB surface with the parent GHB surface. For ε = 0 and θ_T =±30°, the modified and the parent GHB surfaces become the same. There is a trade-off between the accuracy and the ill-conditioning of the yield criterion; based on which the absolute value of θ_T is chosen to be 29.50°. It is noteworthy that except α=0.5, the terms *A*, *B*, and *C* at any specific hydrostatic stress-point do not remain to be constant but become a function of the deviatoric stress.

6.6 RESULTS AND DISCUSSION

6.6.1 Chosen parameters and UBC

The parametric study has been done for various combinations of ring geometry (radius ratio, r_i/r_0), rock mass strength (*GSI*, m_i, σ_{ci}), surcharge loading (q/σ_{ci}), and loading positions on the annular section. Based on few earlier literatures, the parameters are chosen as below:

r_i/r_0= 0, 0.25, 0.5, 0.75 and 0.9; r_0 = 1m

GSI = 10 to 100 with an increment of 10

m_i = 1, 5, 10, 15, 20, 25, 30, and 35

σ_{ci}/r_0 = 125–10000

q/σ_{ci} = 0 and 0.5

Loading positions: L_1, L_2, L_3

The ultimate bearing capacity (UBC), p_u, of ring footing on rock mass is expressed as:

$$p_u = \frac{Q_u}{\pi(r_0^2 - r_i^2)} = \sigma_{ci} N_{\sigma 0} \tag{6.11}$$

where, $N_{\sigma 0}$ is the nondimensional bearing capacity factor for the weightless rock mass, and this parameter is used to represent all numerically computed solutions. It should be noted that $N_{\sigma 0}$ is a function of r_i/r_0, *GSI*, m_i, q/σ_{ci}, and loading configuration; any change in σ_{ci} will straightforwardly linear impact the magnitude of p_u in a linear fashion.

6.6.2 Impact of ring geometry and surcharging

Figures 6.4 and 6.5 present the variation of $N_{\sigma 0}$ with respect to r_i/r_0 corresponding to different values of *GSI*, m_i, and loading position; Figure 6.4 corresponds to no surcharge loading (i.e., q/σ_{ci} =0) and Figure 6.5 pertains to q/σ_{ci} = 0.5. Higher the rock strength parameters higher is the value of $N_{\sigma 0}$; nevertheless, change in *GSI* seems to be more influencing than the variation in m_i. Compare to the L_0 configuration, allowable loading intensity is noticeably higher for any other considered partial load arrangement. Table 6.1 illustrates how the loading position affects the UBC of the ring foundation placed over rock stratum. Amongst the chosen partial loadings, the bearing capacity of ring foundation is maximum for L_1 and becomes least for the L_3 position. The trend of the $N_{\sigma 0}$ profiles with respect to r_i/r_0 also gets significantly impacted by the loading position. Irrespective of the rock strength and the surcharge pressure, when the load application is of L_1 type, the $N_{\sigma 0}$ curves continuously decreases with the reduction in annular section. However, as the hollow section of the ring expands, the curves pertain to L_2 and L_3 type either remains constant or shows increasing pattern up to a certain value of r_i/r_0 and then starts decreasing. In case of L_2 loading without surcharging, the $N_{\sigma 0}$ curves initially increases as the foundation turns from solid circular (r_i/r_0 =0) to hollow ring (till r_i/r_0 =0.25) one; with the presence of surcharge loading this initial increment gets suppressed and results in a horizontal plateau. For low m_i (say, m_i =1), no matter whatever be the surcharge loading and *GSI* values, the bearing capacity profiles, especially for L_2 and to some extent for L_3, remain

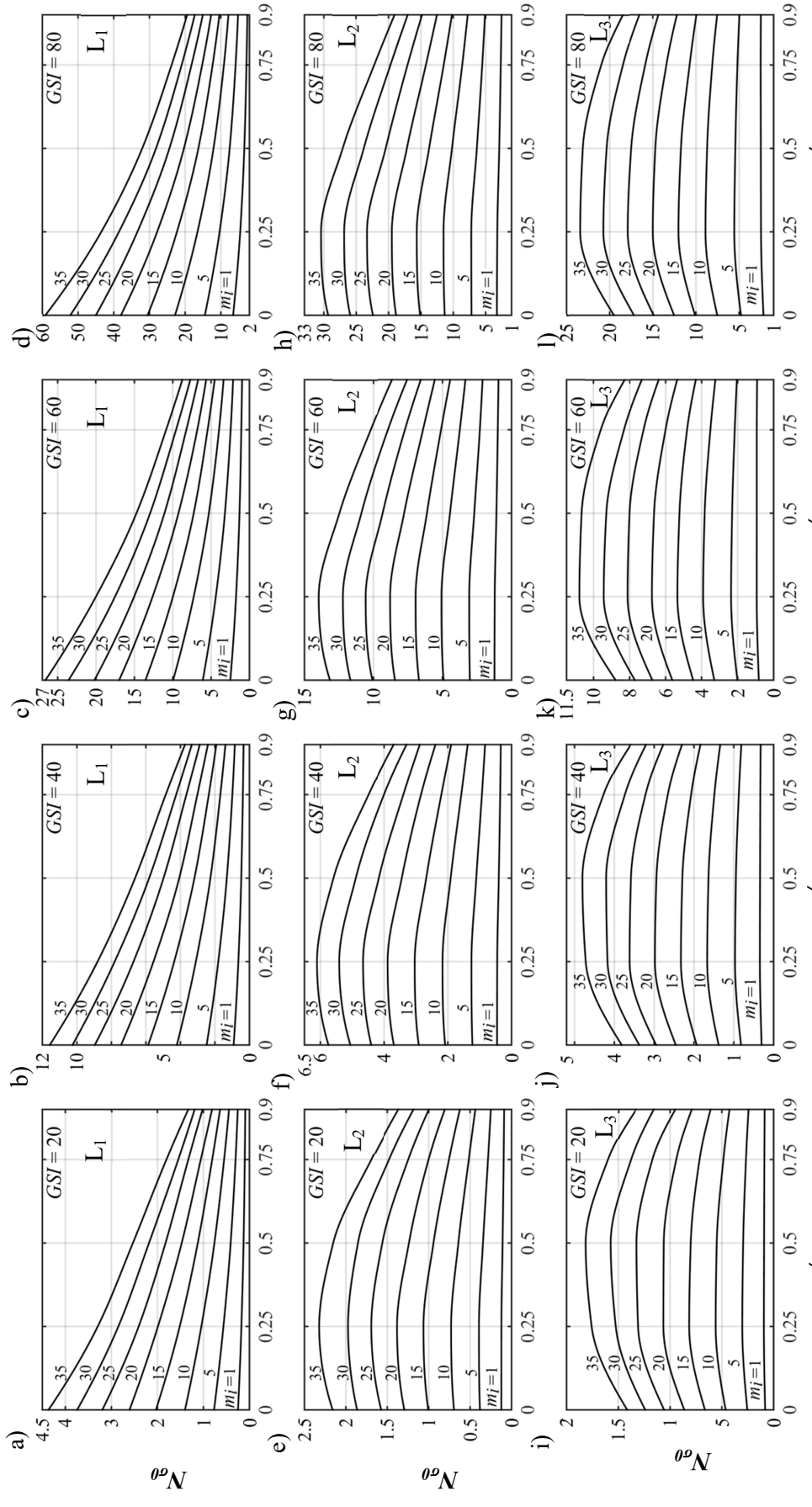

Figure 6.4 The variation of $N_{\sigma 0}$ with respect to r_i/r_0 and m_i corresponding to q= 0 and three different loading positions (a-d) L_1; (e-h) L_2; and (i-l) L_3 and four different values of *GSI*: (a,e,i) *GSI* =20; (b,f,j) *GSI* =40; (c,g,k) *GSI* =60; and (d,h,l) *GSI* =80.

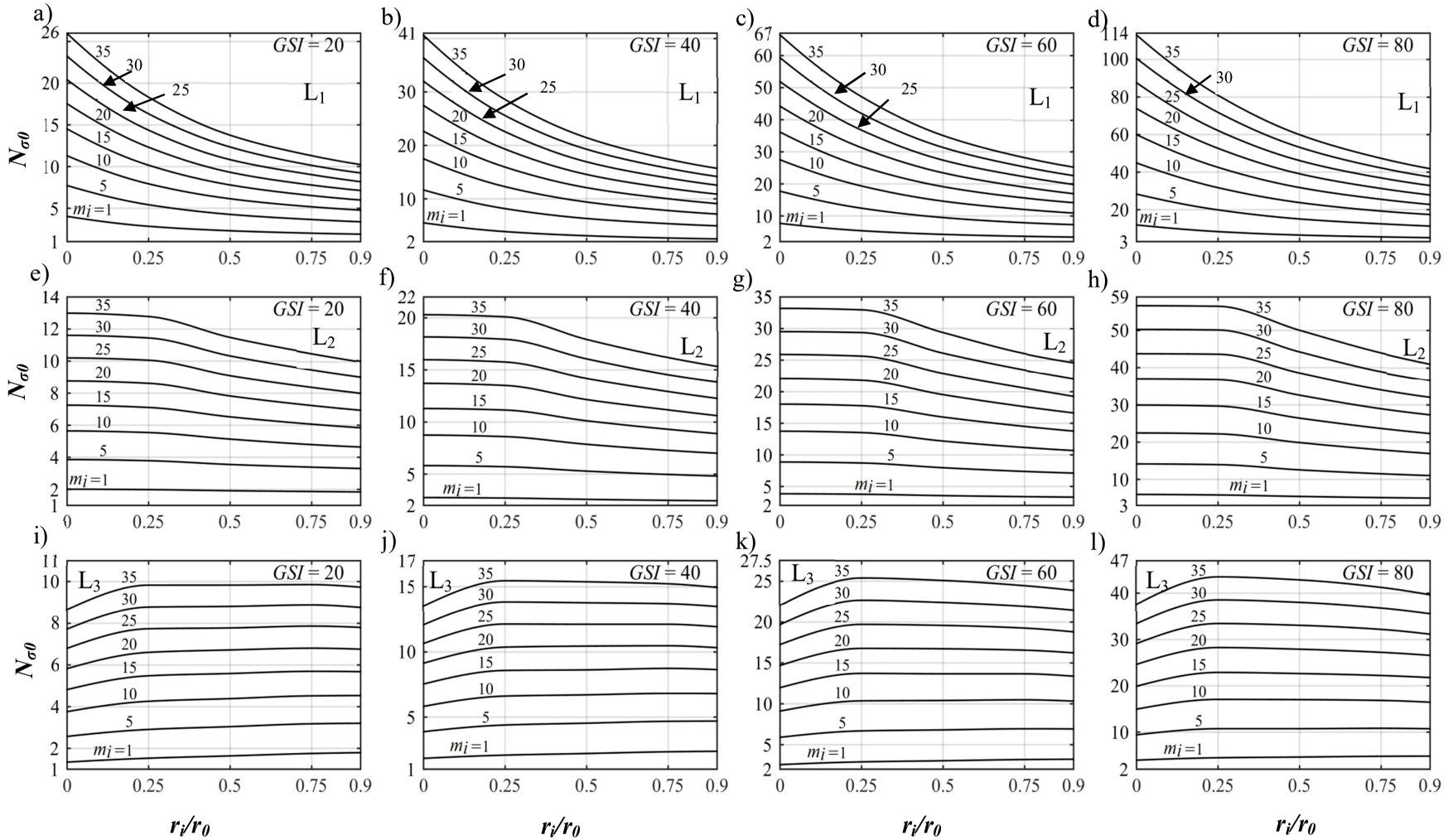

Figure 6.5 The variation of $N_{\sigma 0}$ with respect to r_i/r_0 and m_i corresponding to q= 0.5σ_{ci} and three different loading positions (a-d) L_1; (e-h) L_2; and (i-l) L_3 and four different values of *GSI*: (a,e,i) *GSI* =20; (b,f,j) *GSI* =40; (c,g,k) *GSI* =60; and (d,h,l) *GSI* =80.

Table 6.1. A comparison of $N_{\sigma 0}$ for different loading positions on various rings rested over rocks of different strengths

Load position	r_i/r_0	*GSI*=10				*GSI*=50			
		m_i=10		m_i=30		m_i=10		m_i=30	
		q/σ_{ci}=0	q/σ_{ci}=1	q/σ_{ci}=0	q/σ_{ci}=1	q/σ_{ci}=0	q/σ_{ci}=1	q/σ_{ci}=0	q/σ_{ci}=1
L_0	0.00	0.14	1.19	0.47	3.79	1.67	7.46	4.18	19.01
	0.25	0.15	0.87	0.51	2.81	1.75	5.43	4.59	13.97
	0.50	0.13	0.63	0.46	2.03	1.54	4.01	4.16	10.34
	0.75	0.11	0.48	0.37	1.49	1.30	3.04	3.27	7.71
L_1	0.00	0.55	8.84	1.68	18.51	6.56	21.82	15.71	46.20
	0.25	0.41	6.20	1.28	13.03	4.79	15.33	11.76	32.52
	0.50	0.30	4.84	0.99	9.86	3.51	11.63	8.75	24.42
	0.75	0.21	4.12	0.70	8.13	2.62	9.69	6.46	19.72
L_2	0.00	0.27	4.43	0.83	9.27	3.24	10.92	7.76	23.05
	0.25	0.29	4.34	0.89	9.14	3.34	10.71	8.16	22.82
	0.50	0.25	4.04	0.84	8.26	2.94	9.75	7.34	20.44
	0.75	0.20	3.81	0.66	7.57	2.45	8.97	6.06	18.37
L_3	0.00	0.18	2.94	0.55	6.15	2.16	7.27	5.19	15.36
	0.25	0.22	3.34	0.69	7.01	2.58	8.23	6.33	17.60
	0.50	0.22	3.46	0.72	7.07	2.53	8.36	6.27	17.49
	0.75	0.19	3.58	0.62	7.12	2.31	8.45	5.66	17.23

to be almost unaffected by the size of the annular section; however, for L_1 configuration, even for very weak rocks (lower *GSI* and lower m_i) circular footing is effective than the ring one. Most of the curves generated for L_2 and L_3 type loadings, either yield a prominent peak point or a range of r_i/r_0 ratio at which the p_u value is maximum; the maximum r_i/r_0 ratios that exhibit highest UBC are termed here as critical r_i/r_0, and expressed as $r_i/r_0|_{cr}$. The increase in rock strength and incorporation of overburden pressure exhibits high prominence of $r_i/r_0|_{cr}$ point, especially for L_2 loading.

The attainment of $r_i/r_0|_{cr}$ occurs at relatively wider annular section if the underlying rockmass is quite stronger (i.e. high *GSI*). For L_2 and for L_3 configuration, $r_i/r_0|_{cr}$ occurs between 0.25 to 0.40; surcharging effect and L_3 load enlarges the range of r_i/r_0 where maximum p_u lies. These observations give an impression that the circular footings are preferable for L_1 loading; whereas, for L_2 and L_3 loadings, ring footings are found to be beneficial not only from an economic perspective but also due to the ability of withstanding high load intensity. For relatively weaker rocks with surcharging, even $r_i/r_0 \geq 0.7$ are more effective than the solid circular one if the loading arrangement is of L_3 type.

6.6.3 Impact of rock strength

Figures 6.6 and 6.7 demonstrate how the UBC corresponding to various loading positions gets affected by the rock strength. Figure 6.6 displays the variations of $N_{\sigma 0}$ with m_i values corresponding to various *GSI*, two ring geometries (r_i/r_0 = 0.25 and 0.75) with (q/σ_{ci} = 0.5) and without surcharging (q/σ_{ci} = 0); Figures 6.6a–6.6d pertain to L_1 load type and Figures 6.6e–6.6h present the normalized UBC profiles subjected to L_3 loading. The figures reveal that irrespective of r_i/r_0, q/σ_{ci}, *GSI*, and load type, $N_{\sigma 0}$ increases almost linearly with m_i; however, the slope of these linear envelopes drastically increases with the enhancement in *GSI*. Comparing the results between L_1 and L_3 loadings, it appears that these slopes are unaffected by the load type but reduces to a noticeable extent with the increase in overburden pressure.

Figure 6.7 depicts the trend of the $N_{\sigma 0}$ profiles with respect to *GSI* and corresponding to (a) various radius ratio, (b) two values of m_i's, namely, m_i=5 and m_i=35, and (c) different loading conditions; Figure 6.7a–6.7d and Figures 6.7e–6.7h pertain to L_1 and L_3 load type, respectively. In contrary to the $N_{\sigma 0} - m_i$ curves, the relationship between $N_{\sigma 0}$ and *GSI* produces nonlinear profiles; the profiles typically

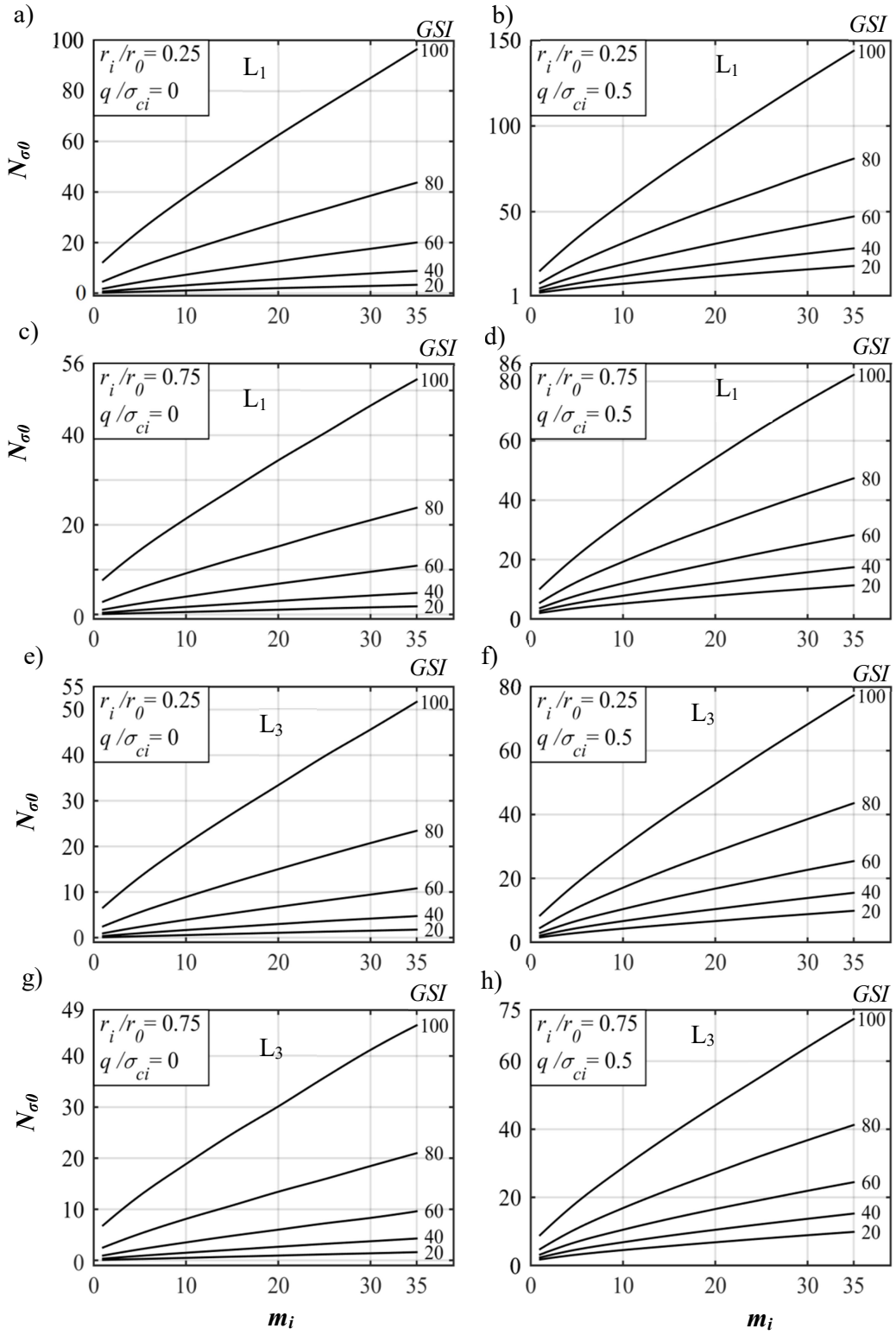

Figure 6.6 The variation of $N_{\sigma 0}$ with respect to m_i for different values of *GSI* and corresponding to (i) various loading positions: (a-d) L_1; (e-h) L_3; (ii) different ring geometries: (a,b,e,f) r_i/r_0=0.25; and (c,d,g,h) r_i/r_0=0.75; and (iii) contrasting surcharges: (a,c,e,g) q/σ_{ci} = 0.0; and (b,d,f,h) q/σ_{ci} = 0.5.

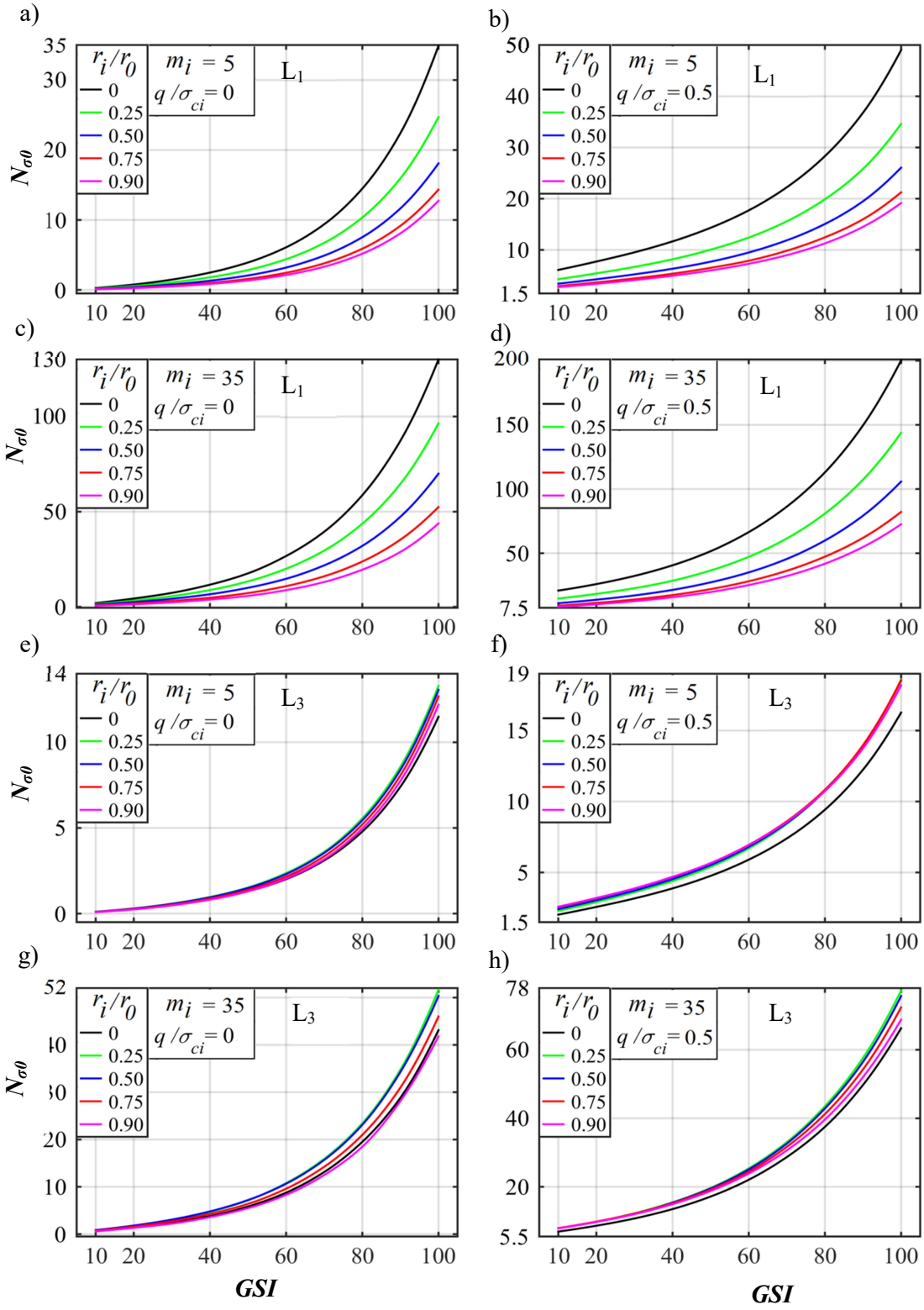

Figure 6.7 The variation of $N_{\sigma 0}$ with respect to *GSI* for different values of r_i/r_0 and correspond-ing to (i) various loading positions: (a-d) L_1; (e-h) L_3; (ii) different m_i: (a,b,e,f) m_i =5; and (c, d,g,h) m_i =35; and (iii) contrasting surcharges: (a,c,e,g) q/σ_{ci} = 0.0; and (b,d,f,h) q/σ_{ci} = 0.5.

appear as convex downward curves. These curves, in a way, displays three specific sectors: an initial gentle slope (for *GSI* < 60), a final steep slope (for *GSI* > 80), and in-between transition curve. It can be interpreted that irrespective of the loading position, the bearing capacity of ring footings enhances manifolds if the *GSI* of the underlying rock is greater than 60. Unlike L_3, the profiles emerging from various sizes of ring footing subjected to L_1 loading are distinctive and unique in nature; the surcharging effect further widens the deviation between these curves. Further, for L_1 loading, the $N_{\sigma 0}$ versus *GSI* profiles corresponding to solid circular footing lies at the top and advances downwardly with the increase in r_i/r_0 ratio. However, for L_3 type of loading, the gap between the $N_{\sigma 0}$ profiles generating from different r_i/r_0 ratio is relatively minimal. Moreover, the curves from the solid circular footing lies at the bottom when the load is of L_3 types; this indicates the ability of ring footing in enduring high load intensity. There is one more striking feature of the surcharging effect on poorer quality rockmass; the surcharge pressure prevents the closeness of $N_{\sigma 0}$ profiles at low *GSI*, irrespective of load types and m_i values.

6.6.4 Failure patterns

The combined effect of material properties, ring geometry, loading position, and surcharge pressure on the overall extent of the failure domain at the collapse state are critically scrutinized. Unlike the Mohr-Coulomb failure criterion, where the radii ratio of the Mohr circles (at the failure and current stress state) is taken as the basis of plotting the failure pattern, in the present chapter, the proximity of shear failure is characterized by the deviatoric stress ratio (*a/d*), as previously mentioned in the work of Chakraborty and Kumar (2015); here, *a* indicates the value of $\ddot{\sigma}$ which is computed at a point from the obtained set of stress ($\sigma_r, \sigma_z, \sigma_\theta$, and τ_{rz}) at the state of incipient

collapse and *d* indicate the $\ddot{\sigma}$ value for which yielding will occur at that specific σ_m and θ. The magnitude of *a/d* lies between 0 and 1; *a/d* =0 indicates no shearing condition, *a/d*<1 represents the non-plastic state of stress whereas, *a/d*=1 indicates the plastic state of failure. The zone which undergoes plastic state of deformation is marked by dark black colour.

Figure. 6.8–6.10 display the failure pattern for various combinations of load arrangements, material properties, ring geometries and variation of surcharge. Irrespective of the considered inputs, a triangular non-plastic trapped zone exists below the footing base. Starting from the tip point of the triangular wedge, a curvilinear plastic zone develops and extends towards the ground surface. The radial distance of the curvilinear boundary surface from the footing edge continuously increases from the tip point to the ground surface. This, in a sense, manifests the log-spiral shape of the failure shape. The lateral spread of the failure zone remains always much greater than the vertical spread. Figure 6.8 depicts the failure patterns for various rings rested over a rock medium having the following properties: *GSI* =90 and m_i=20 and are subjected to three different load alignments. The plastic shear domain in the circular footing apparently looks like a single shear bulb, whereas two distinct shear bulbs arise during the shear failure of ring footings. These shear bulbs are asymmetrical for lower values of r_i/r_0, but with the narrowing of the annular section the shear bulbs approach towards symmetricity; this asserts the fact that for very high r_i/r_0, (say $r_i/r_0 > 0.75$) the ring footing simply behaves like a strip footing. Further, the load type also influences the failure patterns to some extent. The size of the elastic wedge appears to be maximum for the circular footing, especially under the action of L_1–type loading. The plastic failure zone encompasses higher volume of rock medium when the ring footing is subjected to inner half loading. The L_1 loading also enforces gradual reduction in the

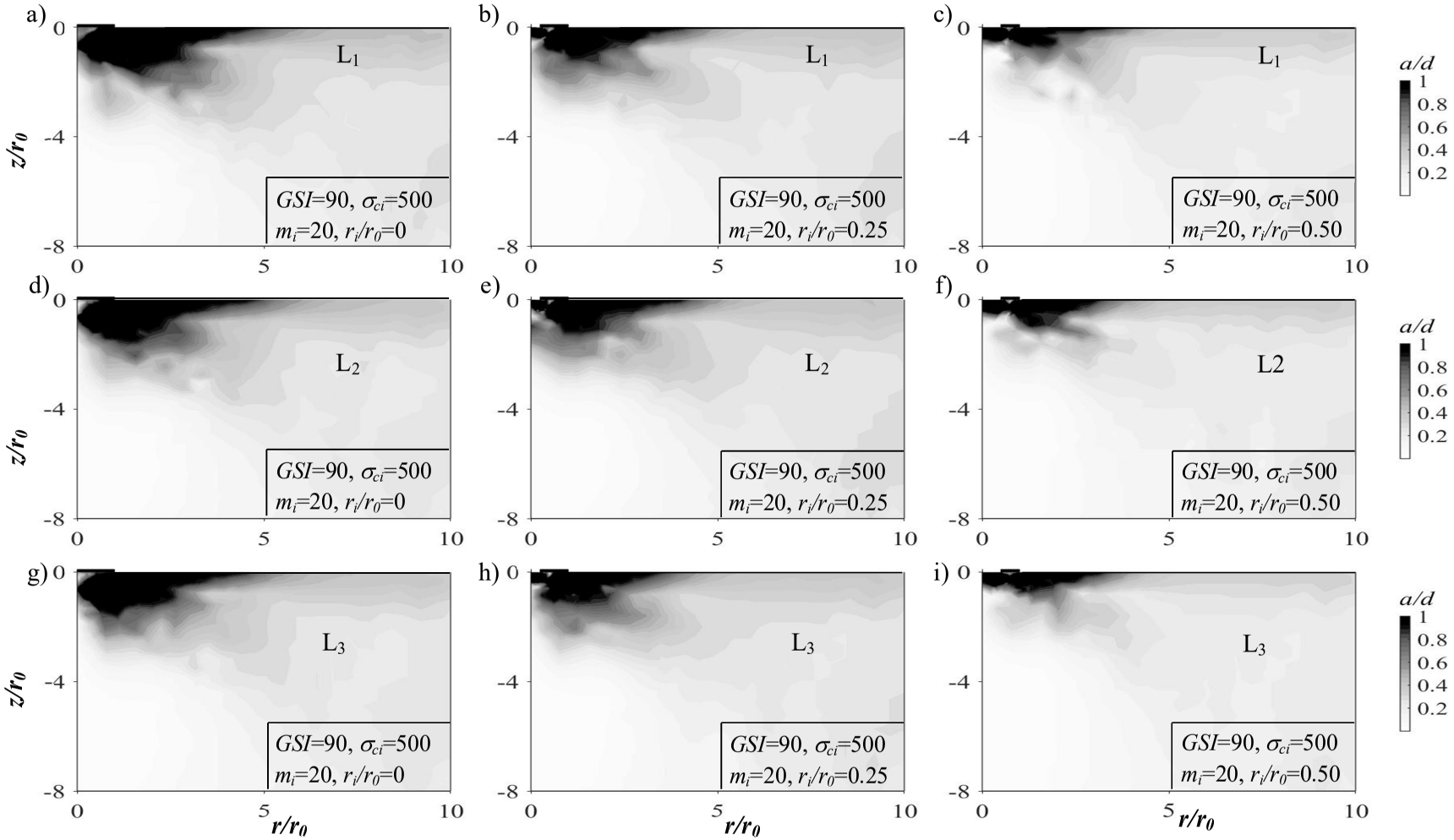

Figure 6.8 Failure patterns developed in the homogenous rocks with *GSI*= 90; m_i= 20; and σ_{ci} =500 for different ring footings of radius ratio (a,d,g) r_i/r_0=0.0; (b,e,h) r_i/r_0=0.25; (c,f,i) r_i/r_0=0.50; and subjected to various loading configurations: (a-c) L_1; (d-f) L_2; and (g-i) L_3.

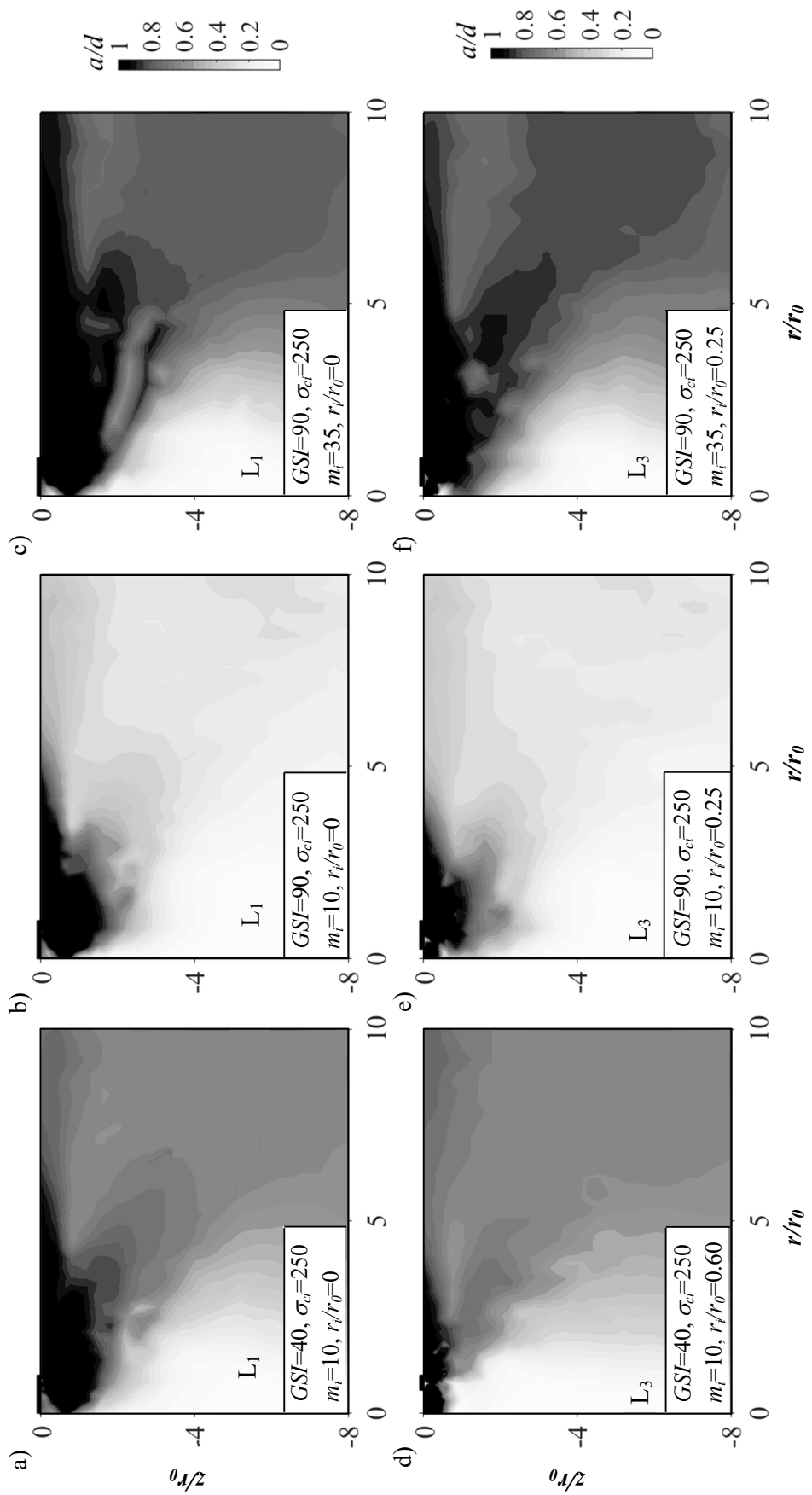

Figure 6.9 Failure patterns developed in the homogenous rocks with varying material properties: (a,d) *GSI*=40; m_i=10; (b,e) *GSI*=90; m_i=10; and (c,f) *GSI*=90; m_i=35; and supporting rings of critical radius ratio subjected to two different loading positions: (a-c) L_1; and (d-f) L_3.

extent of the plastic zone as the ring width decreases. The effect of the material properties on the shear failure zone are presented in Figure 6.9 for L_1 and L_3 type of loading corresponding to $r_i/r_0|_{cr}$. Three different sets of *GSI* and m_i, namely, (40,10), (90,10), and (90,35) are chosen for the purpose of comparative illustrations; the first and the second numbers within the parenthesis indicate the *GSI* and m_i values, respectively.

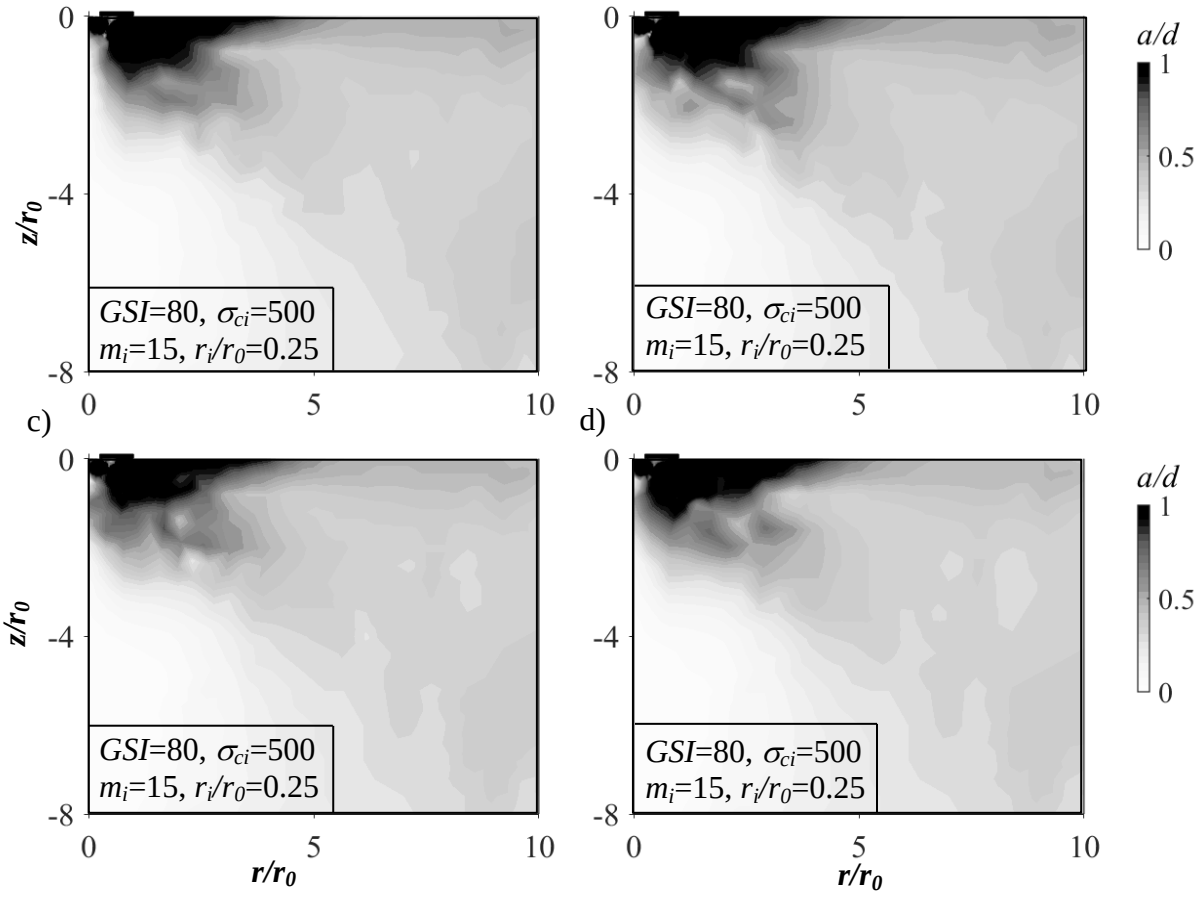

Figure 6.10 Failure patterns developed for ring footing (r_i/r_0= 0.25) rested over homogenous rocks having m_i=15; *GSI*=80; σ_{ci}=500 with different surcharge pressures: (a,c) q= 0.0; (b,d) q= 0.5σ_{ci} ; and different loading conditions, namely, (a-b) L_1; and (c-d) L_3.

Increasing any of the rock strength parameters manifests a marginal curtailment of the elastic wedge, but the change in *GSI* and m_i values exhibits a sharp contrast in the overall size of the plastic shear zone. For high *GSI* and constant m_i, there is an

appreciable diminution in the failure zone, whereas high values of m_i effectuate a remarkable enlargement of the overall volume of the plastic shear zone. The expansion of the failure zone due to increase in m_i occurs primarily along the lateral direction. For very strong rocks, the larger shear bulb does not get contained within the shown reference domain. The curvilinear boundary surface containing the failure zone turns to be smooth and continuous for high *GSI* and relatively low m_i. Comparing the failure domain generated from the rings of critical radius ratio, it can be inferred that the enclosed rock volume within the failure surface is quite higher for inner half loading in comparison to its outer half counterpart. To investigate the effect of surcharge on the size and the shape of the failure domain, the failure contours are drawn with ($q = \sigma_{ci}$) and without ($q = 0$) surcharge pressures for L_1 and L_3 type of loadings applied on ring footing ($r_i/r_0 = 0.25$) rested over weightless rock medium and having the following properties: $GSI = 80$, $\sigma_{ci} = 1000$, $m_i = 15$; Figure 6.10 displays such comparisons. With the increase in surcharge pressure, the plastic shear zone grows in size especially in the lateral direction. The volumetric expansion due to the surcharge pressure is visible more for L_3 loading. Moreover, the discontinuity of the curvilinear boundary of the shear bulb around the edge of the outer ring diameter gets more prominence for the outer half loading. From these figures, it can be apprehended that compare to the loading position and the surcharge pressures, the ring geometry and the mechanical strength of the rock govern the overall development of the failure pattern.

6.7 COMPARISONS OF RESULTS

To verify the effectiveness of the present numerical technique, the bearing capacity factors of solid circular ($r_i/r_0 = 0$) and ring footing ($r_i/r_0 > 0$) rested on homogenous rock are computed and duly compared with the solutions reported in the available literature. Due to non-availability of previous studies regarding partial

loadings, the present comparisons are made only for the case where load is distributed uniformly over the entire plan area (L_0). Tables 6.2 and 6.3 present such comparisons for various rocks. Table 6.2 shows the comparison of N_σ values for circular footing ($r_i/r_0 = 0$) corresponding to different magnitude of *GSI*, m_i, and ($\sigma_{ci}/\gamma r_0$); $\sigma_{ci}/\gamma r_0 = \infty$ represents weightless rock mass. The results obtained in the present study are further compared with the solutions provided by (i) Clausen (2013) on the basis of displacement based elastoplastic finite element method, (ii) Chakraborty and Kumar (2015) with the aid of LB-FELA in association with nonlinear smoothened yield criterion, (iii) Keshavarz and Kumar (2018) by using stress characteristic method, (iv) Keshavarz and Kumar (2018) by using FELA based software Optum G2, and (v) Kumar and Mohapatra (2018) on the basis of the LB-FELA in combination with semidefinite programming (SDP). The

Table 6.2. A comparison of $N\sigma$ values for circular footing ($r_i/r_0 = 0$) using different methods

GSI	$\sigma_{ci}/\gamma r_0$	m_i	Present study[a]	Clausen (2013)[b]	Chakraborty and Kumar (2015)[a]	Kumar and Mahapatra (2018)[a]	Keshavarz and kumar (2018)[c]	Keshavarz and kumar (2021)[d]
10	250	7.5	0.171	0.176	0.694	--	0.174	0.166
20	4000	22.5	0.813	0.851	--	--	0.846	0.78
30	∞	22.5	1.287	1.381	1.87	--	1.351	1.264
40	500	35	3.39	3.544	--	--	3.519	3.231
50	10000	10	1.635	1.678	1.79	1.69	1.661	1.598
60	∞	35	6.76	7.053	6.65	--	6.94	6.507
80	1000	10	5.701	5.818	--	5.12	5.788	5.557
100	500	22.5	23.32	23.91	--	--	23.747	22.858

Note: a: The solutions are obtained on the basis of finite element lower bound theorem by smoothening the yield criterion and using IPM.
b: The solutions are obtained on the basis of Elastoplastic Finite element analysis.
c: The solutions are based on stress characteristic method.
d: The solutions are obtained on the basis of FELA software, Optum G2

present solutions are in well accordance with the LB-FELA solutions that consider the variation of α with *GSI*. In the work of Kumar and Mohapatra (2018), the inclusion of true value of α was done indirectly by varying the material strength parameters. For low *GSI*, α is greater than 0.55; and therefore, an appreciable difference in N_σ value is observed between the present method and the solution of Chakraborty and Kumar (2015) where a constant value of α (α = 0.5) is taken. However, finite element and stress characteristics solutions are on the higher side of the present numerical values. This can be attributed to the lower bound nature of the problem. Moreover, in the stress characteristics method, circumferential stress was considered to be equal to the minor principal stress. Keshavarz and Kumar (2021) validated the stress characteristics solutions with the results obtained from FELA software Optum G2.

Table 6.3 further represents the comparison of $N_{\sigma 0}$ values for ring footing corresponding to different radius ratio (r_i/r_0= 0.25, 0.50, and 0.75) with the solutions provided by Xiao et al. (2020), Keshavarz and Kumar (2021) and Yodsomjai et al. (2021) obtained from OPTUM G2 software. The comparisons are carried out for L_0 type loading with a specific value of *GSI* (=20) and three different m_i's (=10, 20, and 30). The present solutions are slightly lower than the previous studies. This might be due to the conservatism in the bearing capacity factors exhibited by the smoothening of the yield surface. The closeness of the present and previous numerical solutions, for the circular as well as ring footings, provides the necessary confidence in the adopted methodology and the formulations.

Table 6.3. A comparison of $N_{\sigma 0}$ values for ring footing on rock mass.

GSI	m_i	r_i/r_0	Present Study[a]	Xiao et al. (2020)[b]	Keshavarz and kumar (2021)[b*]	Yodsomjai et al. (2021)[b*]
20	10	0.25	0.372	0.384	0.377	0.381
		0.5	0.328	0.337	0.33	0.331
		0.75	0.267	0.273	0.278	0.288
	20	0.25	0.716	0.749	0.77	0.769
		0.5	0.645	0.668	0.663	0.68
		0.75	0.520	0.534	0.56	0.545
	30	0.25	1.062	1.119	1.15	1.16
		0.5	0.964	0.995	0.987	1.004
		0.75	0.803	0.816	0.815	0.82

Note: a: The solutions are obtained on the basis of finite element lower bound theorem by smoothening the yield criterion and using IPM.
b: The solutions are obtained on the basis of FELA software, Optum G2
*:extracted from the graph

6.8 SUMMARY

This study finds out the effect of partial loading on the ultimate bearing capacity of ring footing rested over homogenous rock layer. Three different patterns of partial loading (inner half, middle half, and outer half) are chosen and their affects are duly investigated by extensively varying the rock strength, overburden pressure, and ring geometry. The numerical experimentations are carried out by adopting the finite element lower bound limit analysis in association with nonlinear optimization. To obtain unique values of gradient and Hessian at all the stress state, the three-dimensional generalized Hoek-Brown yield surface, used in this work, is carefully smoothened in the octahedral and the meridian planes. The solution charts are presented in terms of non-dimensional bearing capacity factor and failure contours are drawn in terms of deviatoric stress ratio. Irrespective of any other external factors, the ultimate

load-bearing capacity appears to be higher when the load is being applied on a limited portion rather than the entire plan section; amongst the three chosen partial loadings the maximum UBC is recorded when the external load is applied on the inner half portion. The usage of ring footing becomes highly effective for the outer half loading; nevertheless, for inner half loading, solid circular footing always yields the highest UBC. Based on the rock material, surcharge pressure, and load placement there exist a critical radius ratio at which the footing can withstand the maximum amount of load. The numerical simulations also reveal that the ring footings are highly preferable when the surcharge pressure is present. The obtained solutions are in well agreement with the published literatures.